Chapter 3

Synthesis, characterization, and hetero-photocatalytic studies of $Bi_4Ti_3O_{12}$-$BaTiO_3$ composite

3.1 Introduction

In the contemporary world, pollution and wastewater are the major threat to civilizations. The widespread disposal of industrial wastewater containing organic dyes onto land and water bodies has led to severe contamination in many countries worldwide. About 15-20% of the sum global production of dyes used during the dyeing process, is released into the environment as textile effluent (Naresh and Mandal 2014). Natural anaerobic degradation or chemical degradation of organic dyes yields toxic and carcinogenic products that further alleviates the problem. Therefore, photocatalytic degradation of organic dyes from industrial wastewater is imperative from environmental and health perspectives. Furthermore, freshwater is less than one half of 1% of all the water on earth and the Global rate of water consumption is surpassing the growth rate of the human population. Thus, obligating us to recycle, reclaim and reuse wastewater (Barlow 1999).

Aurivillius family sought great attention in recent years, considering a wide range of dielectric constant and low loss, low coercive field, and good fatigue endurance. These properties have made them potential for applications in various devices like transducer and actuators (Nayak et al. 2015). Other mentionable potentials of bismuth layered pervoskites are in random access memory (RAM), oxygen ion conductors, lead-free relaxor, multiferroics, photoluminescent films and photocatalysts for hydrogen production and water purification (Moure 2018). So we applied a member of this family of oxide here in solving the problem of wastewater. Moreover, this aspect of titania has been used for antimicrobial and sterilizations characteristics (Sunkara and Misra 2008; Venkatasubramanian et al. 2008). So their application is not merely concised to degradation of dye. It can also be promising for photooxidation of microorganism resulting in self-sterilizing and self-cleaning techniques (Rana et al. 2006;

Jagdish Rawat et al. 2007; J. Rawat et al. 2007). This family of materials have fascinated enough owing to its photocatalytic activity in removal of organic and inorganic pollutants from water and also air, eradication of bacteria and cancer cells, photoreduction of N_2 or CO_2 as well as acting as photovoltaic material for harvestation of solar energy (Rana, Rawat, et al. 2005; Rana, Srivastava, et al. 2005).

Such Aurivillius oxides belong to bismuth-layered perovskite ferroelectric materials and these aurivillius oxide semiconductors have lately evoked high curiosity because of their complex layered and unique electronic structure (Kongmark et al. 2012). The Aurivillius phases is composed of alternating layers of $(Bi_2O_2)^{2+}$ units with perovskite-like $(A_{n-1}B_nO_{3n+1})^{2-}$ blocks in between them, where **A** denotes mono, di- or tri-valent ions (K^+, Na^+, Ba^{2+}, Pb^{2+}, Sr^{2+}, Ca^{2+}, Bi^{3+}) and rare earth elements, B represents tetra, penta or hexa valent ions (Ti^{4+}, Ta^{5+}, Nb^{5+}, W^{6+}, Mo^{6+}, etc.) and m=1,2, 3, 4, 5 indicates to the number of BO_6 octahedral amid neighboring $(Bi_2O_2)^{2+}$ layers (Nayak et al. 2015). The compound thus has polarization in two possible directions in which small vector along c-axis switches from the principal direction independently on a-axis, generating anisotropy and resulting in high dielectric constant (Galasso and Kestigan 2007). The layered arrangement not only allows better polarization of charge species but also provide a better possibility for the diffusion and separation of the photoexcited hole–electron pairs compared to other non-layered photocatalysts (Liu et al. 2014). The separation is possible as the reduction and oxidation lattice sites reside in an isolated manner on the edges and faces of the unit ultrathin sheets. The holes generated in the layered photocatalysts are trapped by water molecules present in the interlayer while diffusing to the sheet surface. This accelerated trapping method of holes causes electrons to be easily and efficiently diffused within the unit sheets

before getting to the edges of the sheets (Liu et al. 2010). Additionally, bismuth (Bi) is a p-block element with filled d orbital, and s-orbital of the valence shell (Bi 6s) can hybridize with p-orbital of oxygen (O 2p) generating hybridized valence band (VB), which facilitate the mobility of holes in the VB generated by the photons and improves the photocatalytic efficiency of the Aurivillius oxide (Zhang et al. 2011 May). Also the introduction of Bi^{3+} lone pairs on the A site of Aurivillius structure could assist the distortion of perovskite that is responsible for ferroelectricity in the materials (Benedek 2015). It has been observed that BO_6 octahedra are not as effective as the A-site cations in controlling the dielectric properties owing to small size change in B-cations. However, the conductivity of $Bi_4Ti_3O_{12}$ hinders the polarization that generates difficulty in the application of BTO based commercial devices. Thus, the various other pervoskites materials have been added for the improvement of polling processes. Therefore, tuning of electric properties by compositional modification and size-effect can fulfill the commercial specifications for resistivity, conductivity, compliance, and Curie temperature (Galasso and Kestigan 2007).

Barium titanate ($BaTiO_3$ or BT) is one of the extensively examined ceramic materials by virtue of its piezoelectric, ferroelectric along with excellent dielectric properties. The substantial dielectric constant of $BaTiO_3$ is due to the existence of ferroelectricity in the materials arises from the distortion of TiO_6 octahedra in the crystal structure (Generic et al. 1952). So, here in this work Barium Titanate ($BaTiO_3$) is added in $Bi_4Ti_3O_{12}$ gives rise to a new material $Bi_4Ti_3O_{12}$-$BaTiO_3$ (BTO-BT) which is significantly easy to pole. BTO-BT belongs to the Aurivillius family where m = 4. A-site in the perovskite is occupied by Ba and Bi ion while B-site by Ti ion. Polarization along the c-axis is absent as it is even layered (m = 4). However, there exists

polarization in a-b-axis as perpendicular to the axis there is a mirror plane. Due to the peculiar crystal structure, BTO-BT exhibits anisotropic ferroelectricity, photocatalytic, and electrical properties. Due to the peculiar crystal structure, BTO-BT exhibits anisotropic ferroelectricity, high dielectric properties and impressive photocatalysis.

3.2 Experimental Section

The $Bi_4Ti_3O_{12}$-$BaTiO_3$ nanocomposite was synthesized by a modified solid-state route via three steps.

Firstly, $Bi_4Ti_3O_{12}$ (BTO) was synthesized by the chemical route using analytical grade chemicals Barium Nitrate $Ba(NO_3)_2$ (99% Merck, India), $Bi(NO_3)_3.5H_2O$, TiO_2 (99.5% Merck, India), as the starting materials. In this route, the aqueous solution containing stoichiometric amounts of salt and an equivalent amount of citric acid (99.5% Merck, India) were mixed in a beaker. The obtained solution was heated on a hot plate at 70–80 °C with continuous stirring to evaporate water. After evaporation of water, a fluffy mass was formed, which was further burnt with a sooty flame. The fine powder was made by crushing the ash obtained with the help of mortar and agate. The powder was calcined at 850 °C for 8 h.

Secondly, $BaTiO_3$ (BT) was prepared similarly by another chemical route process using Ba $(NO_3)_2$, TiO_2 (99.5% Merck, India) and an equivalent amount of citric acid (99.5% Merck, India) as the starting materials. The stoichiometric amounts of the salts after purity correction were mixed in a beaker containing double distilled water and citric acid (99.5% Merck, India) of equivalent amount. The consequential reaction mixture was then heated on a hot plate with constant stirring at 70–80°C to evaporate the water and after evaporation, it formed a fluffy

mass, which underwent self-ignition and exhausted a lot of gasses to yield ash. The ash was grounded using agate and mortar to a fine powder. It was also calcined at 850 for 8 h

Thirdly, an equimolar amount of the thus prepared powder of BTO (1 mole) and BT (1 mole) was mixed using ethanol. In this step, we utilize calcined powder of BTO and BT as raw materials to synthesize the $Bi_4Ti_3O_{12}$-$BaTiO_3$ nanocomposite via a new modified solid-state route. The fine powder thus obtained was blended with 2 wt% polyvinyl alcohol (PVA), dried and pressed using a hydraulic press into cylindrical pellets. The PVA binder was later burnt out at 500°C for 2 h. Finally, the nanocomposite pellets were sintered at 900°C for 8 h and further used for characterization and measurements.

3.2.1 Photocatalytic Experiment:

The photocatalytic activity of the synthesized sample (BBTN) was evaluated by examining the aerobic degradation of RhB in solar light. In order to perform the photocatalytic test, 0.6 mg photocatalyst was mixed with 3 ml aqueous solution of RhB (dye concentration 8.38 mg/L) in a quartz cuvette having path length of 1cm. The mixed solution was stirred in the dark for 60 min prior to solar irradiation to achieving adsorption equilibrium. After that, the sample solution was irradiated by solar light. The photocatalytic efficiency of the sample was analyzed by recording the UV-Vis absorption spectra at 554 nm (RhB) at a certain time interval.

In order to identify the active species generated during the photocatalytic experiment, 0.5 mM parabenzoquinone (PBQ), isopropyl alcohol (IPA), and potassium iodide (KI) were added as scavengers for superoxide radicals ($O2^{-}$), hydroxyl radicals ($^{\bullet}OH$), and holes (h^{+}), respectively.

3.3 Characterization

The diffraction pattern of $Bi_4Ti_3O_{12}$-$BaTiO_3$ (BTO-BT) nanocomposite was recorded by X-ray diffractometer (XRD, Rigaku miniflex 600, Japan) using Cu-Kα radiation (λ = 1.54 Å) with 1°/min scan rate. The FTIR spectra of sintered powder was characterized using KBr pellets by ATR FTIR (Bruker, ALPHA model) Spectrophotometer in the frequency range 500–1500 cm^{-1}. UV-visible (UV-Vis) spectrum was examined by a UV-Vis spectrophotometer (UV2600, Shimadzu). The surface morphology of material was analyzed by scanning electron microscope (ZEISS model, EVO18 Germany) whereas its elemental compositions was analyzed by Energy dispersive X-ray (EDX) spectroscopy (Oxford instrument; USA). For particle size determination Transmission electron microscope (TEM, FEI TECANI G2 20 TWIN; USA) was used. The mean particle size and distribution, as well as the zeta potential of the material was determined by a dynamic light scattering technique using a Zetasizer Nano-ZS (Malvern Instruments, Malvern, UK). The Brunauer–Emmett–Teller (BET) surface area was investigated by nitrogen adsorption-desorption isotherm measurements at 77.350K on a Quantachrome NOVA2000E device. The pore size distribution plot was acquired by the Barret–Joyner–Halenda (BJH) model. X-ray photoelectron spectra (XPS) was recorded using PHI 5000 Versaprobe II photoelectron spectrometer (ULVAC-PHI) using Al Kα X-ray beam. Magnetic analyses was performed with a Quantum Design MPMS-3, over a temperature range 5–300 K at applied magnetic field of ±2 T. In addition to this, temperature-dependent field cooling (FC) and Zero field cooling (ZFC) magnetization was recorded at 100 Oe applied field using SQUID VSM dc magnetometer in the same temperature range.

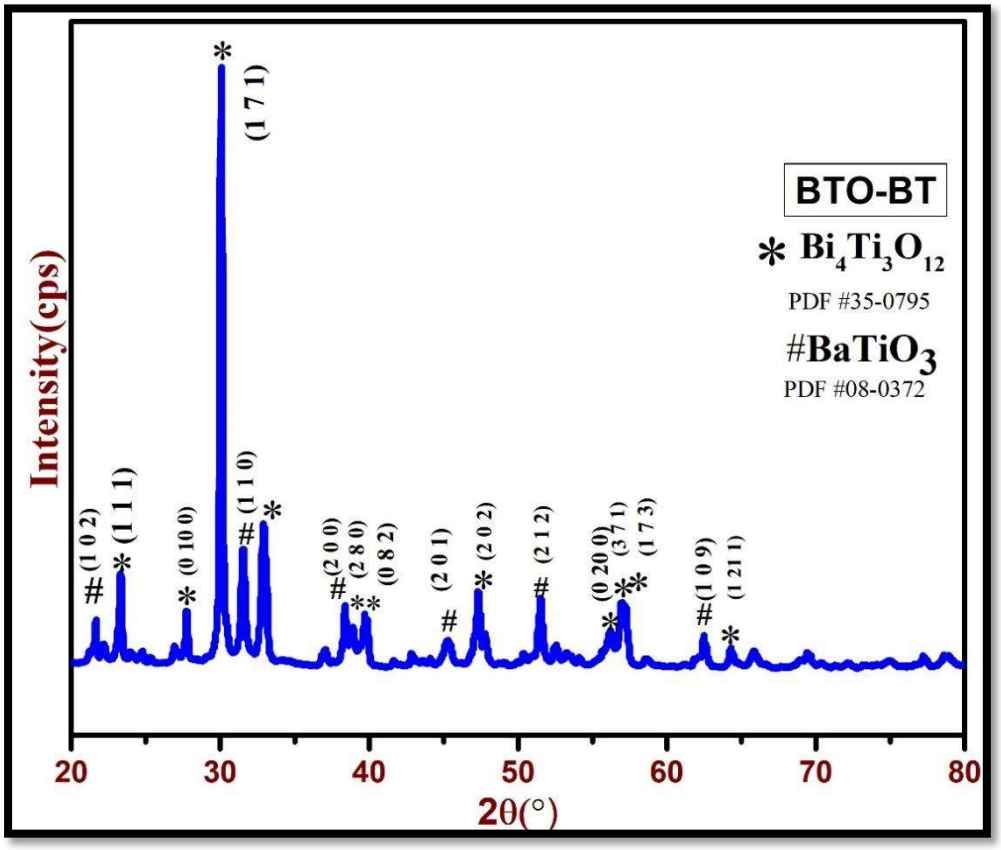

Figure 3.1 indicates high-resolution x-ray diffraction (HR-XRD) patterns of BTO-BT nanocomposite sintered at 900 °C for 8 h.

3.4 Results and Discussion

The figure confirmed the formation of BTO-BT nanocomposite. All the diffraction patterns of XRD results correctly matched with JCPDS card no (35-0795, 08-0372) for BTO-BT composite. The crystal structure for BTO-BT composite having an orthorhombic and cubic structure with space group: Aba2 and Pm-3m, respectively for $Bi_4Ti_3O_{12}$ and $BaTiO_3$ phases. The average crystallite size was calculated by taking five intense XRD peaks of the materials using the Debye-Scherrer formula.

$$D = \frac{k\lambda}{\beta \cos\theta} \tag{3.1}$$

where, k refers to shape coefficient, value of which taken as 0.99, θ is the diffraction angle, λ is the wavelength of X-ray and peak width of the diffraction peak at half-maxima (FWHM) in radians is β. Instrumental broadening cause diffraction peak for crystallite size with respect to standard silicon sample, the corrected value of it is also β.

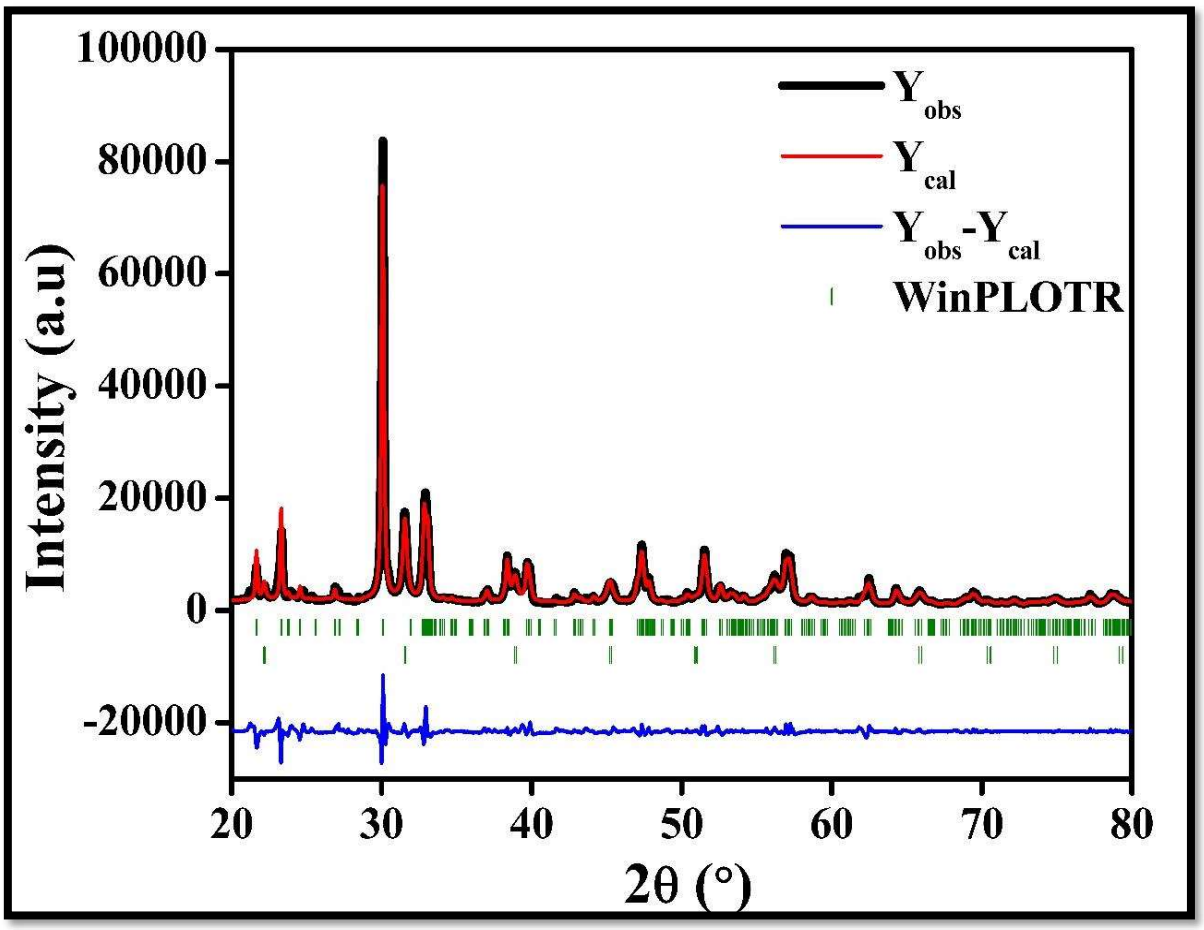

Figure 3.2 Le-Bail fitting of BTO-BT nanocomposite, in which black line represents calculated data, the red line indicates experimental observed data and the blue line represents the difference between observed and calculated ($(Y_{cal} - Y_{obs})$ data.

Le-Bail analysis of BTO-BT nanocomposite was performed by using Fullprof software in the 2θ range from 20° to 80° is shown in figure 3.2. The observed data (Y_{obs}) indicated by red color line

exactly overlapped with experimentally calculated data (Y_{cal}) represented by the black color line. The lower value of χ^2, expected weight factor (R_{exp}), Weight profile factor (R_{wp}), Braggs R-factor (R_B) for BTO-BT nanocomposite enlisted in Table 3.1 confirms the best fitting of the XRD results (Tellier et al. 2004).

Table 3.1 Refined lattice parameters and space group of BTO-BT nanocomposite sintered at 900 °C for 8 h.

$\chi^2 = 4.96$	R_p: 13.9	R_{wp}: 17.2	R_{exp}: 2.89
Phase 1:	$Bi_4Ti_3O_{12}$	Phase 2:	$BaTiO_3$
Phase	Orthorhombic	Phase	Cubic
Space group	A b a 2	Space group	P m -3 m
Lattice Parameter	a = 32.820419 Å b = 5.416634 Å c = 5.450912 Å	Lattice Parameter	a = 4.009870 Å b = 4.009870 Å c = 4.009870 Å
Angle	α = **β** = γ = 90°	Angle	α = **β** = γ = 90°
Bragg R-factor	1.627	Bragg R-factor	0.6733
RF-factor	0.9515	RF-factor	0.3908

Figure 3.3 shows the FTIR spectra of BTO-BT composite sintered at 900 °C for 8 h, recorded in the frequency range 500–1500 cm^{-1}. Bands appear at 822 and 582 cm^{-1} are associated with metal- oxides bonds. The peak observed around 550 cm^{-1} is due to the presence of M-O (Ti-O) bond vibration, is the characteristic peak of $BaTiO_3$ (Sun et al. 2007; Kumar et al. 2018). The peaks obtained at 1435 cm^{-1} corresponds to metal-oxide-metal bonds (Gordani et al. 2014). All the peaks observed in the FTIR spectra confirm the formation of BTO-BT composite

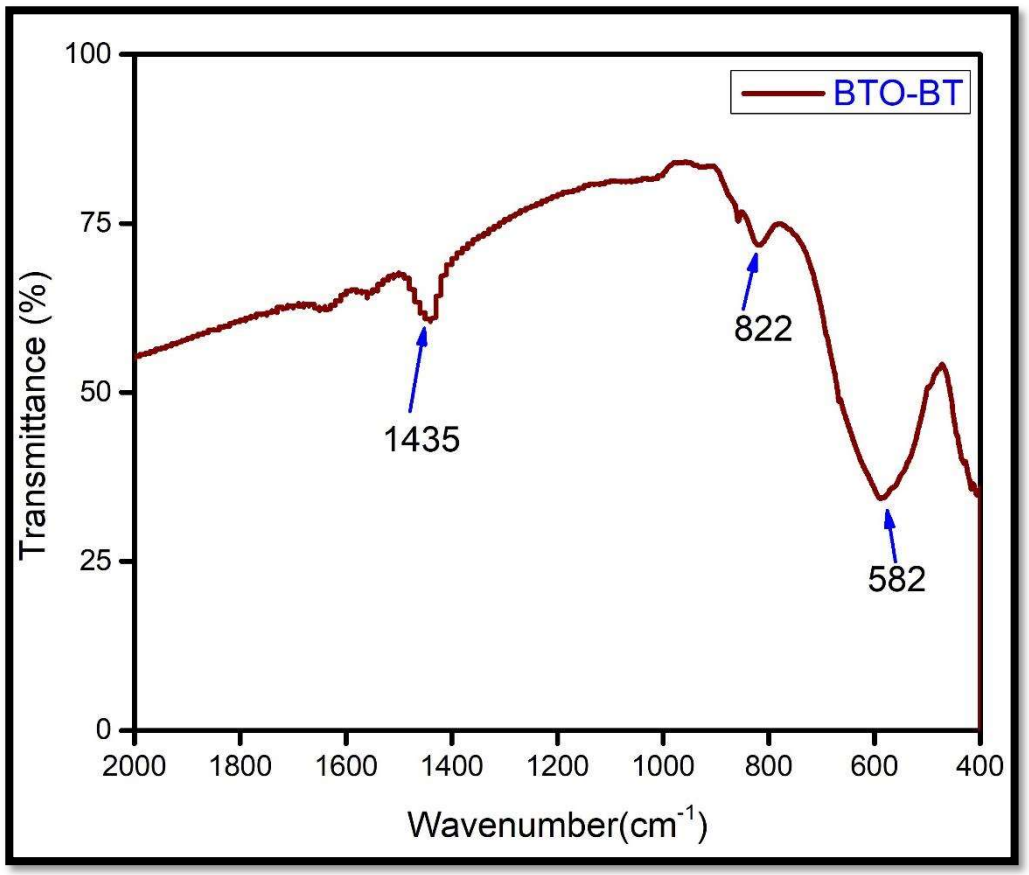

Figure 3.3 FT-IR spectra BTO-BT nanocomposite.

The selected area diffraction (SAED) pattern of the BTO-BT shows bright spot patterns indicates corresponding planes (1 0 9), (1 1 0), (1 1 4), (2 1 1), (1 1 14) , (2 0 0) and (2 1 17) which mentioned in figure 3.4(a). The zone axis of the diffraction pattern between (1 0 9) and (1 1 0) plane is found to be [$\bar{9}$ 9 1]. All the planes obtained from HR-TEM and SAED pattern are similar to XRD, which supports the orthorhombic as well as the cubic nature of the BTO-BT nanocomposite. High-resolution imaging by TEM is shown in figure 3.4(b), corresponding planes of BTO-BT having inter-planer d = 5.23 Å, 6.63 Å are (0 0 8) ,(0 0 6) planes, respectively. Bright-field TEM images of the BTO-BT nanocomposite sintered at 900 °C for 8 h

are shown in figure 3.4(c), confirms the crystalline nature of the particles. The average particle size observed by TEM analysis is 88 ±2 nm for BTO-BT nanocomposite. The observed particles size obtained by TEM measurement for both materials is larger than average crystallite size observed by XRD results, the reason of this can be attributed to the formation of particles with the combination of few crystallites.

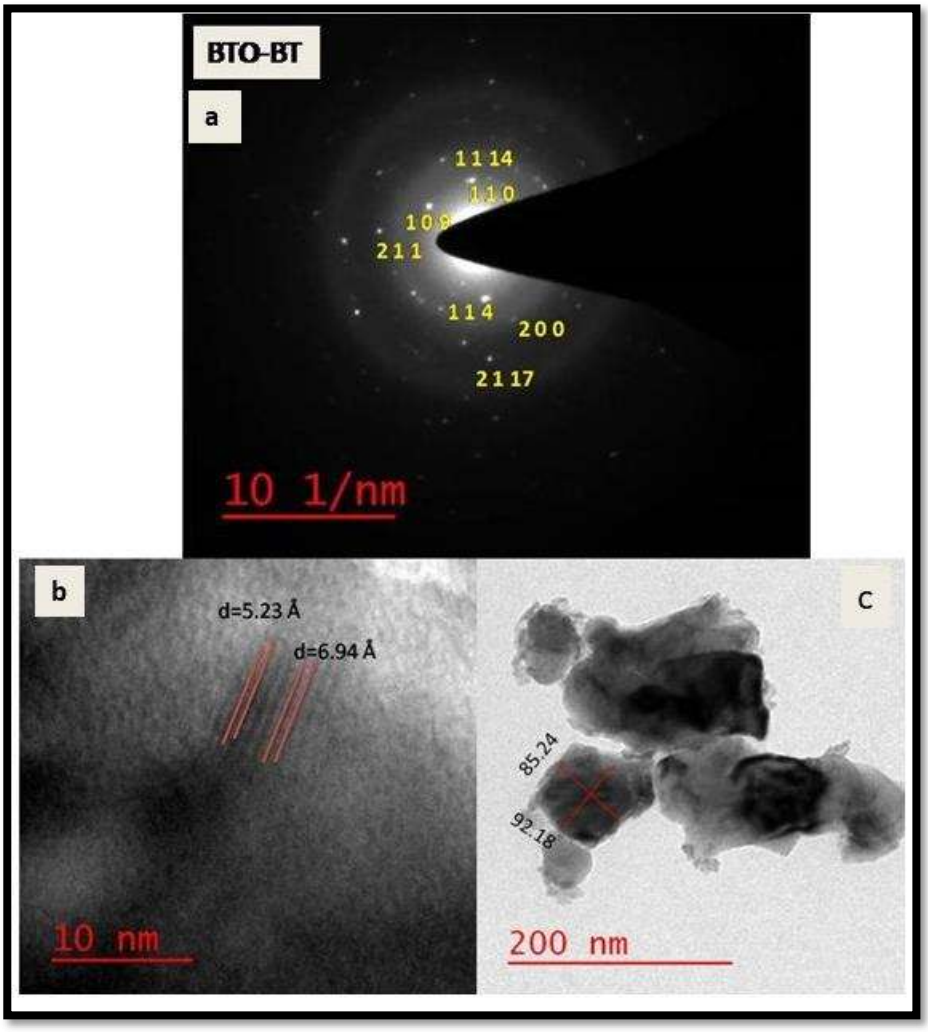

Figure 3.4 (a) SAED patterns (b) HR-TEM images showing d-spacing, and (c) Bright Field TEM Images of BTO-BT nanocomposite.

The surface morphology of both the materials was observed on the gold-coated surface BTO-BT nanocomposite is depicted in figure 3.5(a) reveals the presence of grains separated by grain

boundaries. Heterogeneous surface morphology was witnessed in BTO-BT nanocomposite, indicating bimodal grain size distribution, where smaller grains are dispersed among larger grains having grain size in the range of 211.87 - 455.97 nm.

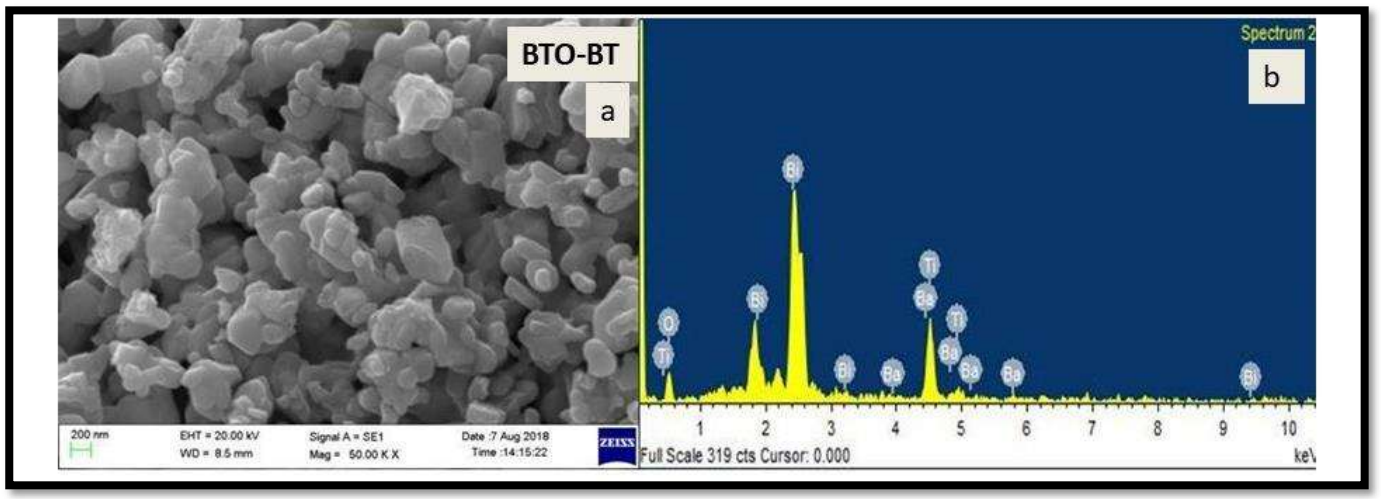

Figure 3.5 (a) SEM micrograph, and (b) EDX spectra of BTO-BT nanocomposite.

The average grain size obtained for BTO- BT nanocomposite is calculated and found to be 275.25 nm. SEM analysis witnesses a larger average grain size than that of crystallite size obtained from XRD measurement as former is formed by aggregation of the latter.

figure 3.5(b) illustrate EDX spectrum for BTO-BT nanocomposite, which reveals the presence of Ba, Bi, Ti, and O elements in BTO-BT nanocomposite which confirms the purity of materials.

The particle size of the material was determined by dynamic light scattering. Figure 3.6 depicts the formation of two peaks indicating bimodal particles, with the mean particle size being 52.8 nm (polydispersity index [PDI] = 0.278. The zeta potential value is a crucial particle characteristic as it can influence both particle stability as well as particle properties. Theoretically, more pronounced zeta potential values, being positive or negative, tend to stabilize particle suspension (Shukla et al. 2013 Apr). The electrostatic repulsion between particles with

the same electric charge prevents the aggregation of the sphere (Feng and Huang 2001). In the present study, zeta potential was −20.7, as can be seen in figure 3.7, the negative value of zeta potential for the material indicating the formation of the stable nanocomposite.

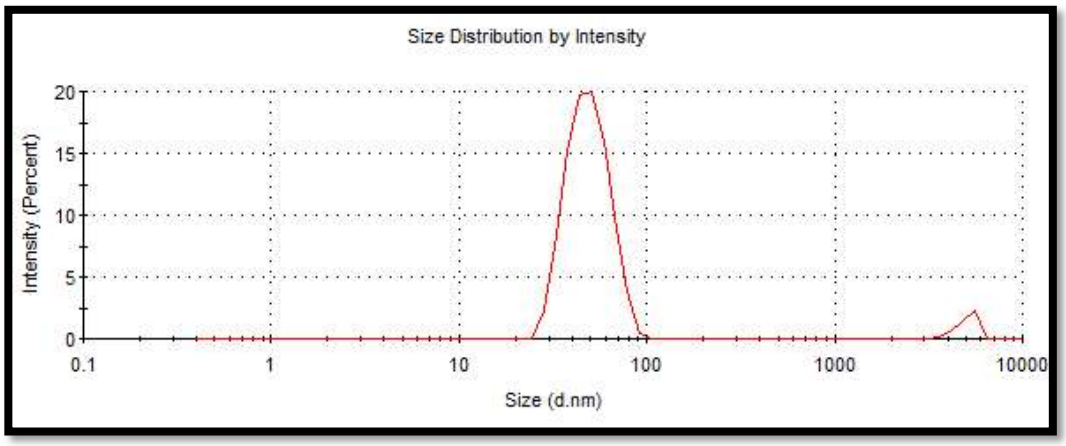

Figure 3.6 Particle size distribution of BTO-BT nanocomposite

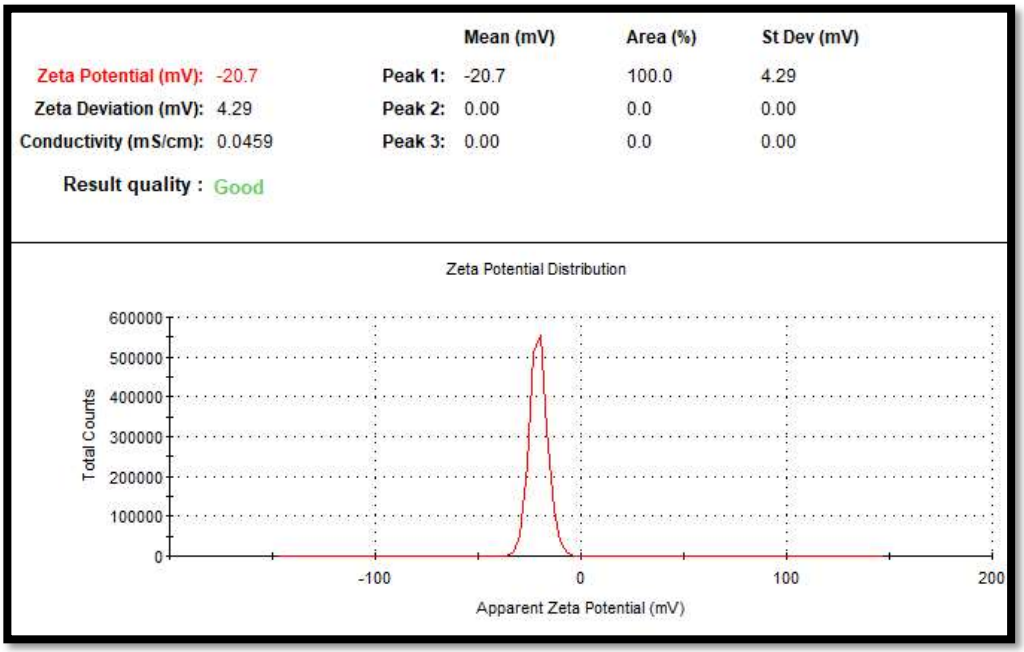

Figure 3.7 Zeta potential distribution of BTO-BT nanocomposite

AFM analysis of BTO-BT nanocomposite was done using tapping mode is depicted in figure 3.8. Histogram of grain size of particles is shown in Figure 3.8(a), indicating that most of the grains are in size range of 0.4-0.6 um in BTO-BT nanocomposite, which is in accordance with SEM and TEM results. Comparable grain size with clear grain boundaries is observed in 2-dimensional AFM images BTO-BT nanocomposite is explained in figure 3.8(b). The distributions of particles on the surface are illustrated by 3-dimensional AFM image on the scanned area of 20 μm x 20 μm in figure 3.8(c). The observed value of average roughness (Ra), root mean square roughness (Rq), maximum profile peak height and maximum profile valley depth for 3-dimensional image of BTO-BT nanocomposite are mentioned in table 3.2.

Table 3.2 Data of AFM analysis received for BTO-BT nanocomposite sintered at 900 °C for 8 h

Average roughness (Ra)	122 nm
Root Mean Square roughness (Rq)	171 nm
Maximum Profile Peak Height	382 nm
Maximum Profile Valley Depth	441 nm

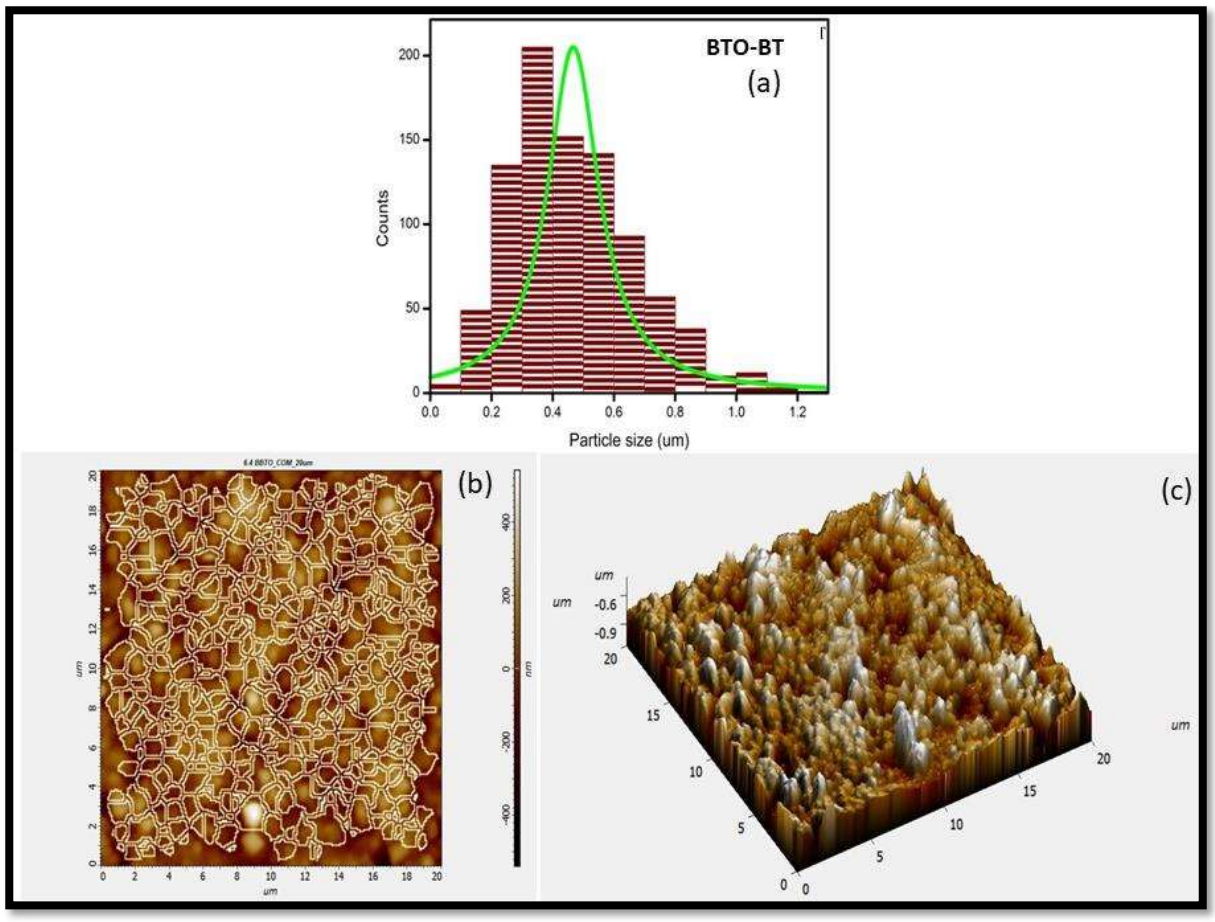

Figure 3.8 (a) Histogram graph for the particle size distribution, (b) 2-D watershed images for grain boundary and (c) 3-D for surface roughness of BTO-BT nanocomposite.

For the detection of oxidation of individual elements that exist in the materials and electronic environment of the elements in BTO-BT nanocomposite, X-ray photoelectron spectroscopic (XPS) analysis was performed (Bantawal and Krishna Bhat 2018). For specimen surface charging correction of the binding energies obtained from the XPS analysis, the C1s line (284.6 eV)was taken as reference. Figure 3.9(a)–(d) portrays the high-resolution XPS spectrum of the material. The presence of elements such as bismuth, barium, titanium and oxygen in BTO-BT nanocomposite were confirmed. High-resolution XPS spectra of bismuth can be deconvoluted into two peaks reveals the existence of Bi^{+3}. Peaks assigned at 159.1 eV and 164.5 eV binding

energies is due to Bi $4f_{5/2}$ and Bi $4f_{7/2}$, respectively (Hou et al. 2013; Zhao et al. 2019). In Figure 9(b), the two peaks at 793.65 eV and 778.35 eV could be assigned to the splitting of the Ba $3d_{3/2}$ and Ba $3d_{5/2}$ spin states, respectively (Panchal et al. 2017). The Ti 2p XPS spectrum shown in Figure 3.9(c) can be deconvoluted into three peaks. Two peaks out of which are characteristic of Ti(IV) at 457.9 due to Ti $2p_{3/2}$ and 463.5 due to Ti $2p_{1/2}$ while

the third one at 465.9 eV, corresponds to the binding energies of Bi $4d_{3/2}$. In the vicinity of 464.5

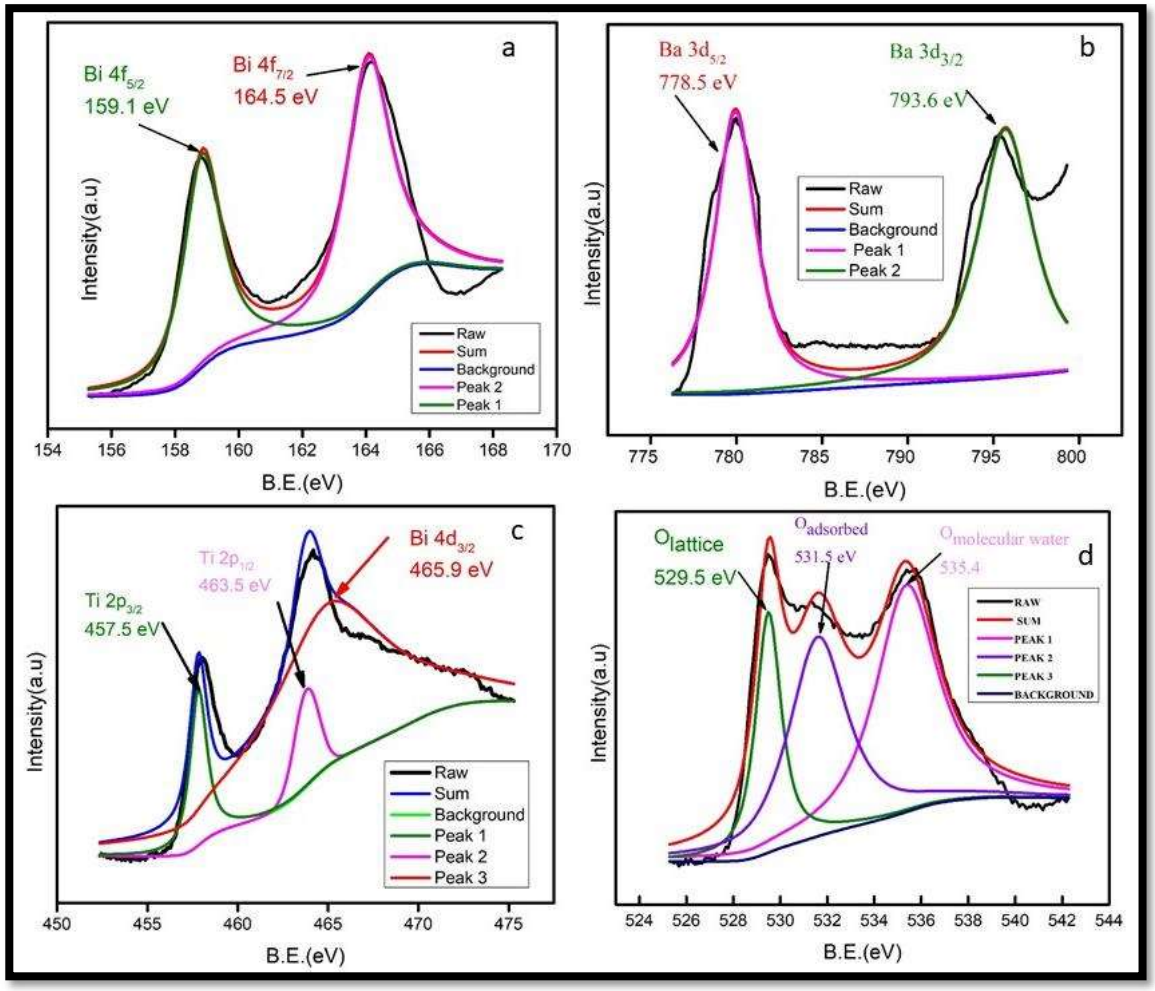

Figure 3.9(a)–(d) High-resolution XPS spectra of the BTO-BT nanocomposite.

eV broad hump is perceived owing to partial overlap between the peaks of Bi 4d3/2 and Ti 2p1/2 (Chu et al. 2002; Hou et al. 2013). A wide and asymmetric spectrum of O 1s is evident from ifgure 3.9(d), inferring the existence of more than one type of O chemical state in the material. This asymmetrical O1s spectrum can be deconvoluted into three components: surface lattice oxygen ($O_{lattice}$) species at binding energy 529.5eV, surface adsorbed oxygen ($O_{adsorbed}$) species at binding energy 531.5 eV, and surface adsorbed molecular water at binding energy 532.8 eV. Higher concentration oxygen species adsorbed at the surface would facilitate enhancement in catalytic activity (Arandiyan et al. 2013; Hou et al. 2013).

3.5 Magnetic studies

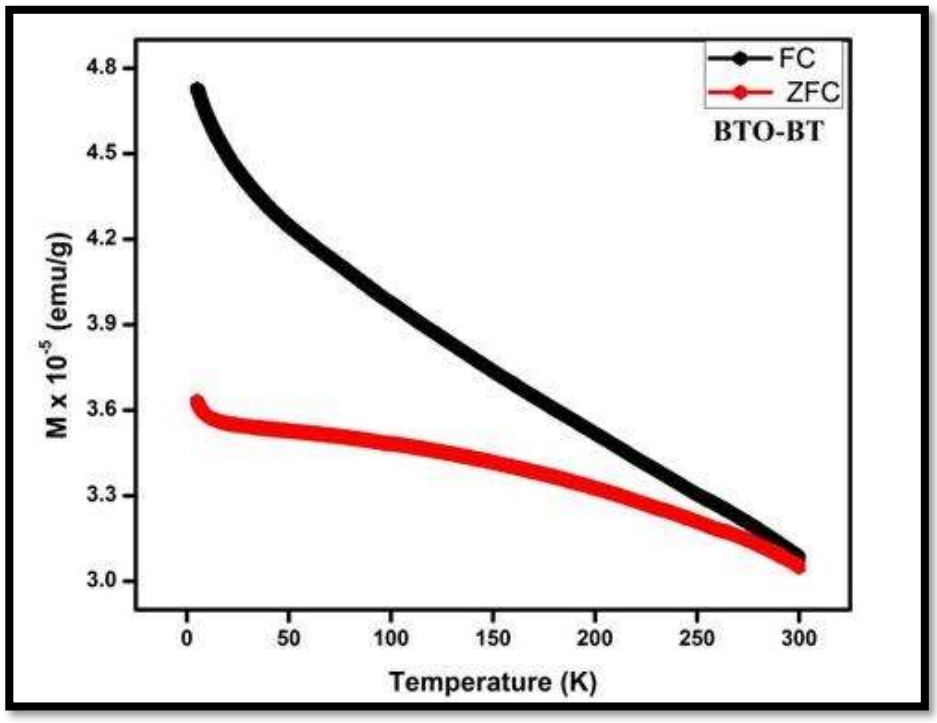

Figure 3.10. Temperature-dependent ZFC and FC at H= 100 Oe BTO-BT nanocomposite.

The dependence of magnetization as a function of temperature was studied during cooling from room temperature (300 K) to the very low temperature (5 K) at a constant applied field of 100 Oe. It is noticed from Figure 3.10(a) that at lower temperature magnetization curve of field cooled (FC) and zero field cooled (ZFC) shows the vast difference. This substantial difference implies that material is frustrated systems, which means that instead of distinct long-range order, there is a heterogeneous mixture of ferromagnetic and anti-ferromagnetic ordering (Sultan et al. 2015). The average of interactions like canted spins structure, thermally induced disorders, ferromagnetism and anti-ferromagnetism cause frustrated spin system leading to anomalous behavior of magnetization with temperature.

It is evident from the figure that both FC and ZFC increase in magnetization with decreasing temperature and exponentially increases at lower temperatures. Monte Carlo suggested that at lower temperatures, disordered spins align themselves along an axis normal to the surface of material, inferring to an exponential increase in the net magnetic moment (Chakrabarti et al. 2013).

Materials are expected to be diamagnetic, as all the comprising elements Bi, Ba, TiO_2 are diamagnetic in nature (Delekar et al. 2012) and same has been confirmed by the plot of measured magnetization versus applied magnetic field (M-H) curve shown in figure 3.11 using Superconducting Quantum Design MPMS Magnetometer Interference Device (SQUID) observed at ±2 T for 5 to 300 K.

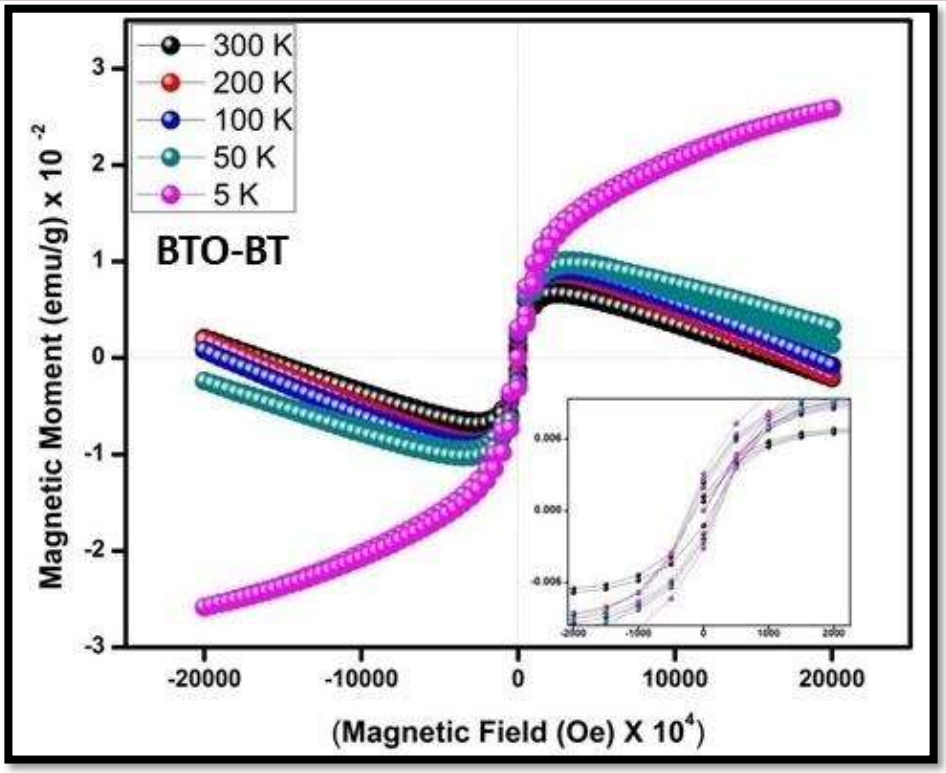

Figure 3.11 M-H hysteresis loop from 5 K to 300 K for BTO-BT nanocomposite.

Howbeit at 5 K a small loop of ferromagnetism is observed at the low magnetic field due to local defects states as can be seen in the inset of figure (Bhattacharya et al.). However, the diamagnetic background is superimposed onto the ferromagnetic loop, suggesting that total magnetic susceptibility embodies both diamagnetic and ferromagnetic parts. Ferromagnetism is dominated at a very low temperature of 5 K (Yoon et al. 2018). The shift observed on the loop can be attributed to spin flop, which corresponds to the reversal of magnetic super lattices and their orientation is oppositely aligned with the magnetic field (May et al. 2014).

3.6 Electrical and Impedance studies

It is a beneficial approach for examining the electrical characteristics of polycrystalline materials and their correlation with microstructures. Along with it, it imparts information regarding the concurrent existence of multi-polarization processes and their relaxation behaviors. The adequate contribution of electrode interface, grains and grain boundaries to the total

capacitance and resistance can also be evaluated (Wang et al. 2017). Three semicircular arcs obtained in the Nyquist plot (imaginary part of impedance(Z") versus real part of impedance (Z')) represents these contributions.

Figure 3.12 shows the Nyquist plot of BTO-BT nanocomposite sintered at 900^0 C for 8 h. In both cases, only two semicircular arcs are evident due to the contribution of grain boundaries and electrode surface effects. The inset in the figures exhibits data at higher frequency and on extrapolation of arc on Z′ axis, the intercept does not find to pass through origin implying the presence of another arc in higher frequency region that is beyond the range of measurement. The intercept obtained at Z′ axis is resistance offered by grains (R_g). The resistance exerted by grain boundaries (R_{gb}), the grain capacitance (C_g) and grain boundary capacitance (C_{gb}) were calculated and mentioned in table 3.3. The impedance offered by the grains and grain boundaries is expressed by the following equations (Kumar et al. 2018).

$$Z^* = \frac{1}{R_g^{-1}+i\omega C_g} + \frac{1}{R_{gb}^{-1}+i\omega C_{gb}} = Z' - iZ'' \quad (3.2)$$

Where, $$Z' = \frac{R_g}{1+(\omega R_g C_g)^2} + \frac{R_{gb}}{1+(\omega R_{gb} C_{gb})^2} \quad (3.3)$$

And $$Z'' = R_g\left[\frac{\omega R_g C_g}{1+(\omega R_g C_g)^2}\right] + R_{gb}\left[\frac{\omega R_{gb} C_{gb}}{1+(\omega R_{gb} C_{gb})^2}\right] \quad (3.4)$$

where, R_g is grain resistance, R_{gb} is grain boundary resistance, C_g and C_{gb} are the capacitance of grain and grain boundary, respectively and ω is angular frequency. The repressions of grain's contribution were due to larger contribution of grain boundaries. It is observed from the Table 3.3 that the value of grains for BTO-BT nanocomposite are lower than that of grain boundaries,

which justifies the semiconducting nature of grains with insulating grain boundaries, as explained by Inter-barrier layer capacitance (IBLC) mechanism.

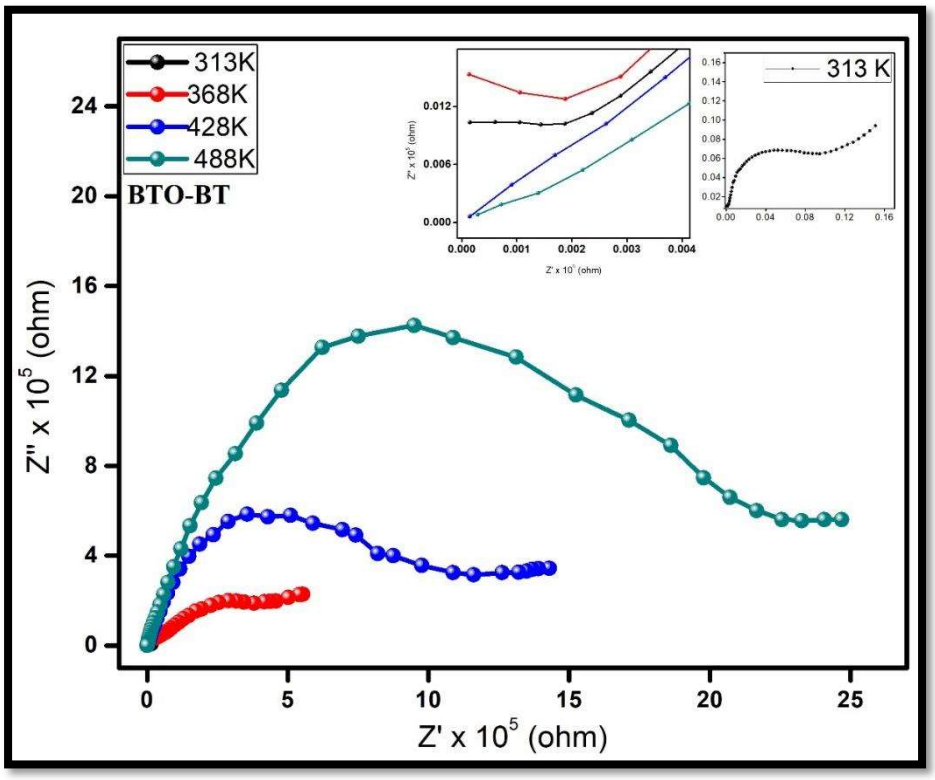

Figure 3.12 Nyquist plots in a range of temperature (313 K-488 K): a BTO-BT nanocomposite. The inset is exhibiting an enlarged view of the higher frequencies.

Table 3.3 The resistance and capacitance exerted by grain boundaries and grains of BTO-BT nanocomposite.

TEMPERATURE (K)	**BTO-BT**			
	R_g (Ω)	C_g (pF)	R_{gb}(Ω) x 10^5	C_{gb} (pF)
313	187.5	0.013	0.095	4.996
368	105.52	0.999	3.79	0.386
428	90.581	0.012	10.84	0.102
488	71.926	0.015	22.53	0.151

Figure 3.13(a) shows the frequency-dependent real part of impedance at few selected temperatures for BTO-BT nanocomposite while the frequency-dependent imaginary part of impedance measured at same temperatures is depicted in figure 3.13(b). Similar trends are observed in both the plots, the magnitude of Z' and Z" inverse relationship with frequency, implying an increase in ac conductivity (Thomas et al. 2017). The relaxation peaks observed at lower frequency regions and at higher frequency regions are due to the contribution of electrode and grain boundary effects, respectively.

Suppression and shifting of relaxation peaks occurring at higher frequency regions provide evidence for the existence of temperature-dependent Maxwell-Wagner dielectric relaxation phenomenon as can be seen from the inset of figure 3.13(b).

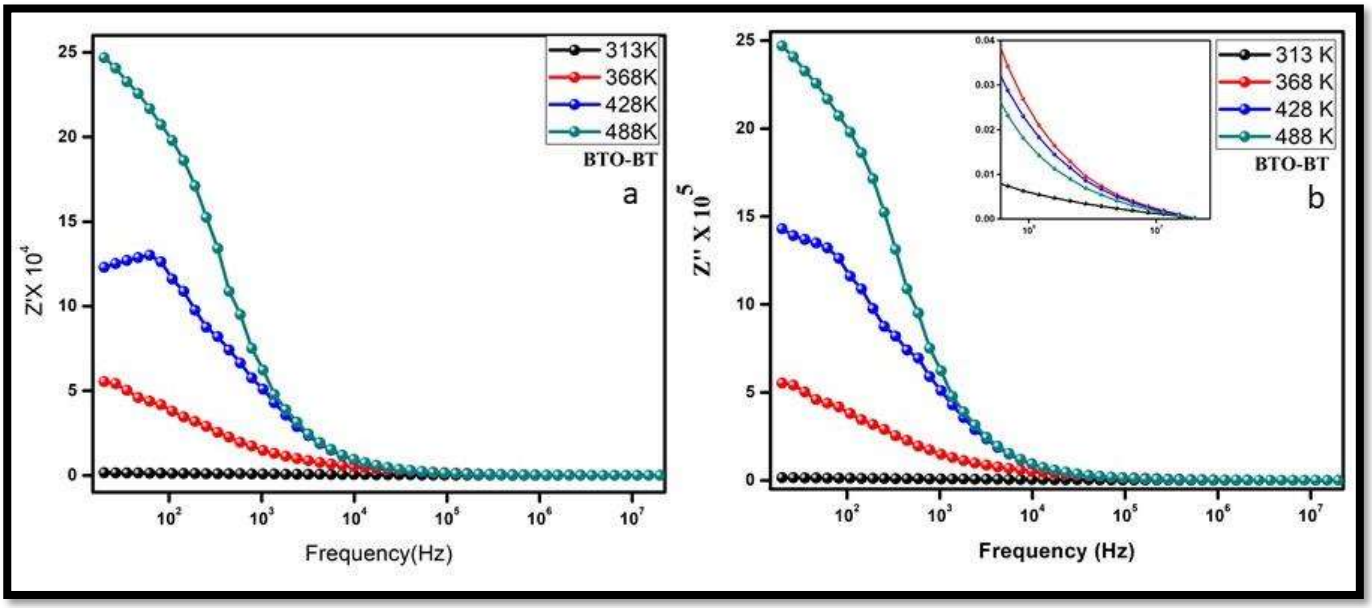

Figure 3.13 (a) represents plot of the real part of impedance as a function of frequency at different temperatures and (b) Plot of the imaginary part of impedance as a function of frequency at different temperatures for BTO-BT nanocomposite.

Dependence of normalized imaginary part (Z"/Z"max) of impedance on the frequency at different temperatures in BTO-BT nanocomposite is shown in figure 3.14. Single relaxation

peaks observed, which is slightly shifted towards higher frequency region with an increase in temperature, this slight mismatch in peak frequency indicates short-range movement of charge carriers which directs

toward thermally activated non-Debye like relaxation process (Ke et al. 2010; Thomas et al. 2017). A short tail in lower

frequency range is observed at 368 K, which may be due to the contribution of electrode and grain

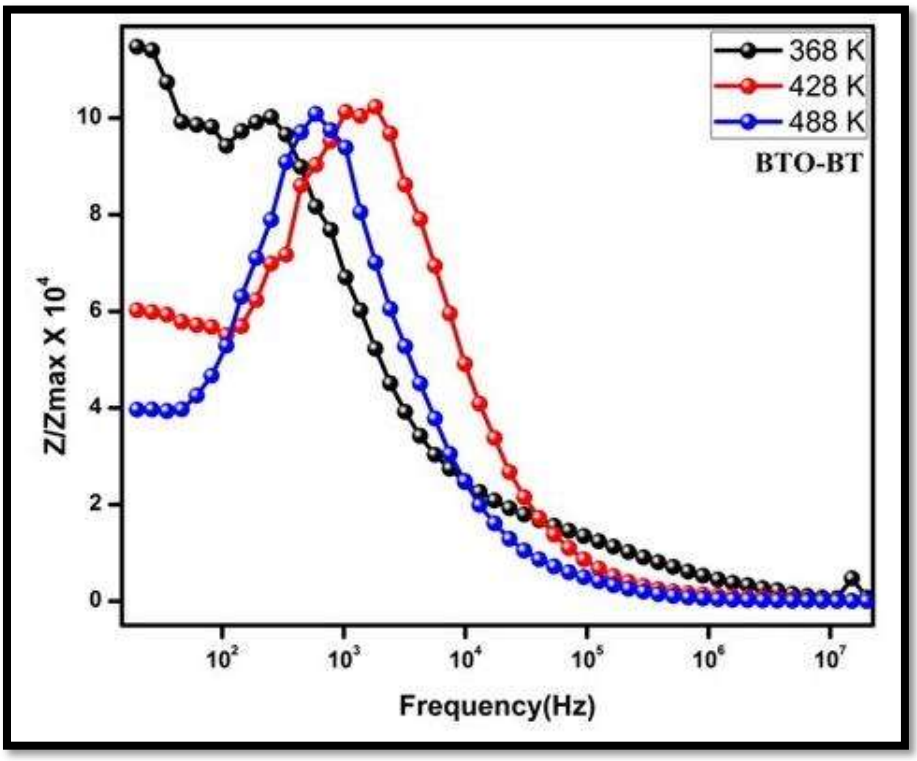

Figure 3.14 Normalized imaginary part of impedance as a function of frequency for BTO-BT nanocomposite

boundary that offers larger resistance in BTO-BT nanocomposite.(Zhang et al. 2018) Peak obtained at higher frequency range highlights the character of grain resistance while the peak at lower frequency highlights the character grain boundaries.

Temperature-dependent conductivity of BTO-BT nanocomposite,at different frequencies is illustrated in figure 3.15(a). Variation of conductivity with temperature is explained by the Arrhenius equation (Wang et al. 2017). –

$$\sigma = \sigma_0 e^{\frac{-\varepsilon_a}{kT}} \quad (3.5)$$

However, the trend of plot obtained is unusual and the reason for such a pattern can be attributed to the effect of lattice scattering (Henini 2010). Where,

$\mu \propto T^{\frac{-3}{2}}$ and $\sigma = eN\mu$, therefore,

$$\sigma \propto T^{\frac{-3}{2}} \quad (3.6)$$

σ - Ionic conductivity; σ_0 - pre-exponent factor; T – Absolute temperature; k – Boltzmann constant; ε_a – Activation energy for ionic conduction; e- electronic charge; N-number of charge carriers; μ- ionic mobility

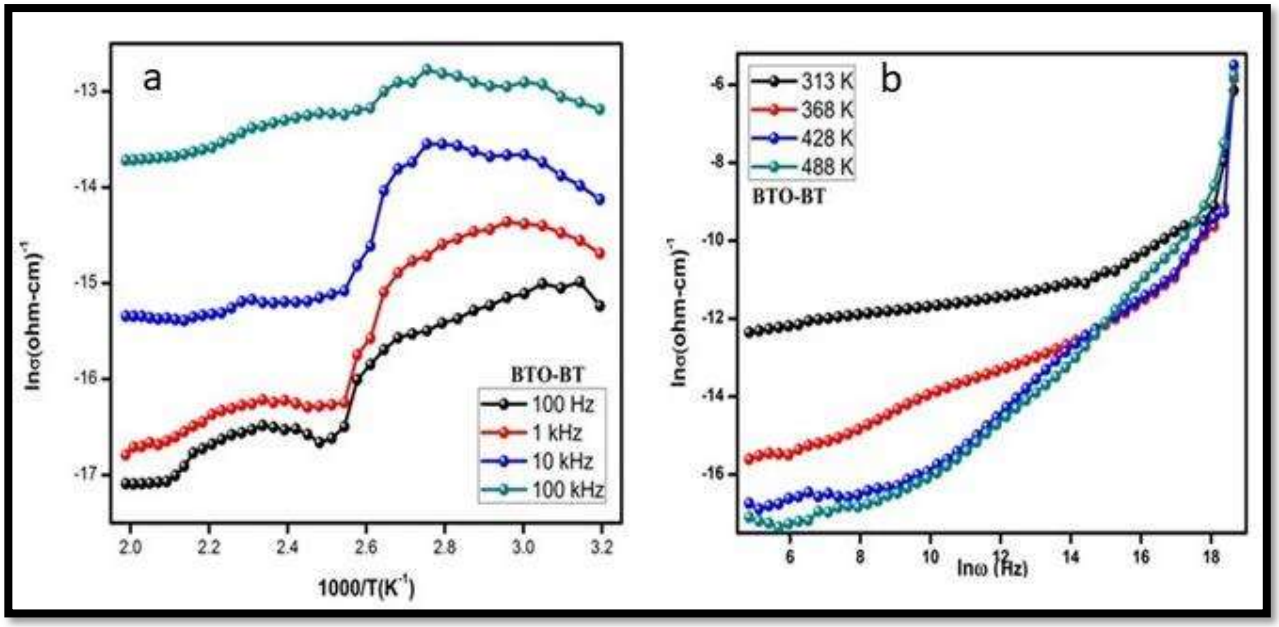

Figure 3.15 (a) AC conductivity with respect to inverse of temperature at different frequencies and (b) Frequency dependent AC conductivity at different temperatures for BTO-BT nanocomposite.

Figure 3.15(b) depicts the dependence of AC conductivity of BTO-BT nanocomposite, on frequencies at different temperatures. It is perceived from the figure that the materials follow a similar trend. At lower frequency, conductivity is predominantly temperature dependent while at higher frequency is more frequency driven. Hitherto it has been established that frequency driven ac conductivity is mainly a consequence of hopping charge carrier conduction, which is less prominent at lower frequency range. The charge carriers are assumed to move in discontinuous jumps "hopping" among well-defined localized sites present within the solids. Here in the present case, we obtain a region where conductivity is a monotonically increasing function of frequency is well fitted by "Joscher's universal power law."

$$\sigma_{ac} \propto \omega^n \quad (3.7)$$

Where n is the power law exponent whose value lies in the range 0 < n < 1. The obtained value of power-law exponent found for BTO-BT nanocomposite is shown in table 3.4.

Table 3.4 The value of power-law exponent found for BTO-BT nanocomposite from the plots shown in figure 3.15(b).

Temperature	313 K	368 K	428 K	488 K
BTO-BT nanocomposite	0.49	0.44	0.63	0.75

These values also rule out the possibility of Debye-type relaxation as for Debye-type relaxation value of the power-law exponent is near to 2 and confirms the Maxwell-Wagner effects caused by a thin oxide layer on the electrode (Jonscher 1972).

3.7 Dielectric Studies

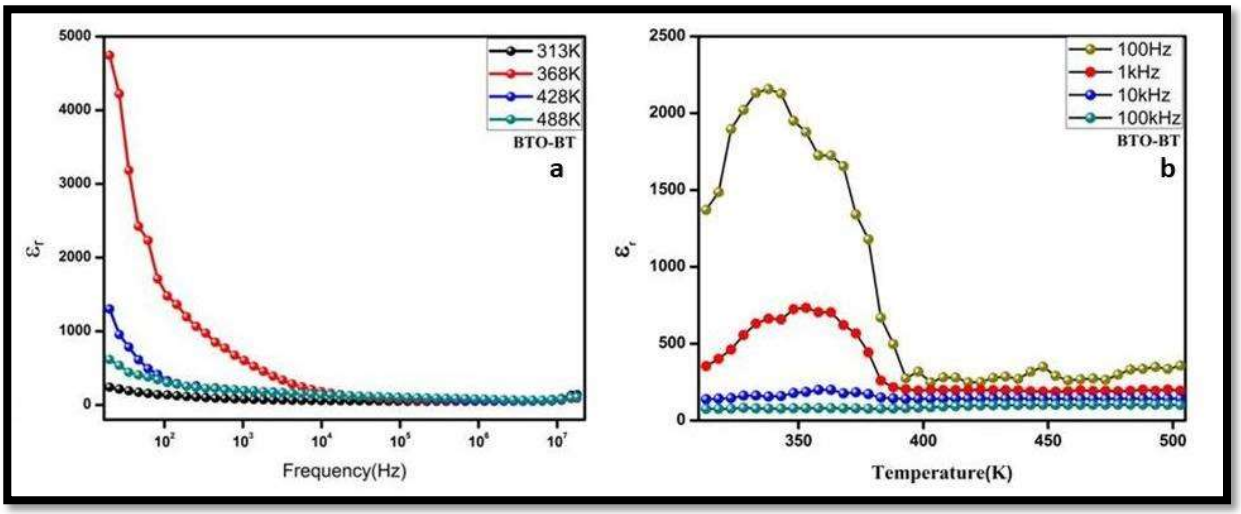

Figure 3.16 (a) Dielectric constant (ε_r) as a function of frequency and (b) - Dielectric constant (ε_r) as a function of temperature for BTO-BT nanocomposite.

The frequency dependence of dielectric constant for BTO-BT nanocomposite at four different temperatures is illustrated in Figure 3.16(a).

It can be realized from the figure that dielectric constant decreases on an increasing frequency. However, the decrease in low frequency range is steep, the reason for this can be attributed to the accumulation of space charge at the interface resulting in the occurrence of polarization of ionic medium. On the other hand, due to the rapid recurrent switch of field, charge accumulation is prevented at a higher frequency side thus as a consequence, almost constant value of the dielectric constant is witnessed (Sharma et al. 2014). The value of dielectric constant obtained for BTO-BT nanocomposite was 4746 at 100Hz and 368 K .

Figure 3.16(b) depicts the variation of dielectric constant with the temperature at different frequencies for BTO-BT nanocomposite. Like typical ferroelectric materials, these materials also undergo phase transition from ferroelectric to paraelectric at which maxima of dielectric appear and temperature corresponding to it is Curie temperature. At 100 Hz, BTO-BT nanocomposite refers to the maximum peak value at 2156. However, in present cases, phase transition are frequency dependent, so the maxima shift with the frequency which exhibits the presence of diffuse phase transition confirming the relaxor ferroelectric behavior. This shift can be explained by modified Curie-Weiss law (Zn et al. 2017).

$$\frac{1}{\varepsilon} = \left(\frac{T - T_m}{C}\right)^{\gamma} \tag{3.8}$$

ε - Dielectric constant; T - temperature; T_m – shift in maximum temperature; C - Curie temperature

If γ = 0 then it remains frequency independent but if γ> 0 then it shows diffuse behavior, which means transition temperature is frequency dependent.

A positive affirmation for relaxor behavior of BTO-BT nanocomposite is derived from the dependence of the imaginary part of dielectric constant (ε”) on frequency as illustrated in figure

3.17. Humungous value of ε" is spotted at a lower frequency that decreases steeply with an increase in the frequency. Through the results of impedance spectroscopy, it has been established that in the dielectric material, high dielectric constant and low dielectric constant coexists, respectively at grains and grain boundaries.

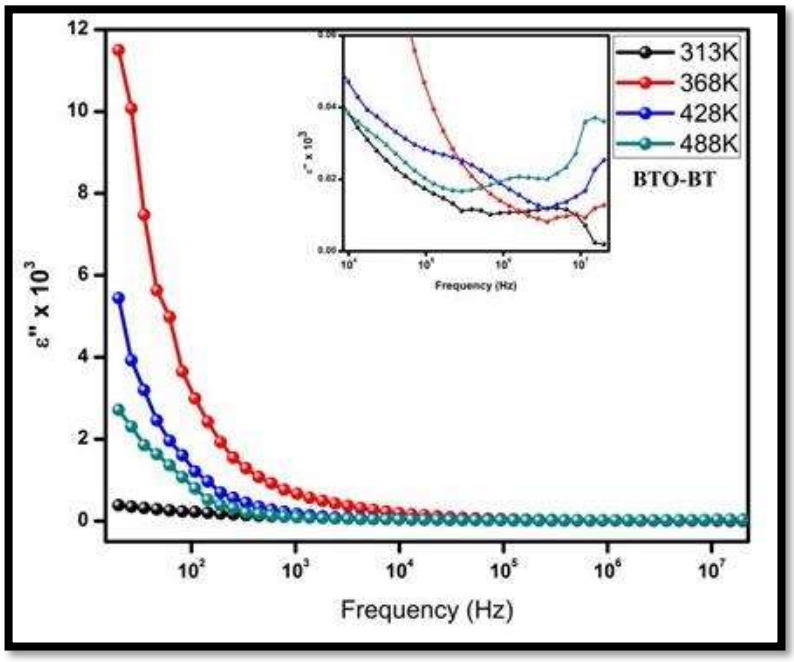

Figure 3.17 The imaginary part of dielectric constant (ε") as a function of frequency for BTO-BT nanocomposite.

Consequently, this dielectric homogeneity can influence the charge accumulation at the interface leading to Maxwell-Wagner (MW) interfacial polarization.(Wang et al. 2017) The infection point obtained in this plot is similar to plot Z" versus frequency giving a clear indication for the existence of Maxwell-Wagner relaxation.(Sharma et al. 2015) It is lucid from the inset in the figure that relaxation was encountered even at higher frequency range that again supports the

presence of Maxwell-Wagner relaxation. Relation of ε" with frequency can be explained by Maxwell-Wagner equation -:

$$\varepsilon'' = \frac{1}{\omega c_0 \left(R_{gb}+R_g\right)} \frac{1-\omega^2\tau_{gb}\tau_g+\omega^2\tau\left(\tau_{gb}+\tau_g\right)}{1+\omega^2\tau^2} \tag{3.9}$$

where

$$\tau_g = C_g R_g \; and \; \tau_{gb} = \; C_{gb} R_{gb} \tag{3.10}$$

$$\tau = \frac{\tau_{gb}R_g+\tau_g R_{gb}}{R_{gb}+R_g} \; ; C_0 = \varepsilon_0 \frac{A}{t} \tag{3.11}$$

where subscript gb and g represents grains boundaries and grains, respectively, τ is the relaxation time, ω is the angular frequency, A and t are area and thickness of the cylindrical pellet.(Wang et al. 2017)

Figure 3.18(a) illustrates the variation of dielectric loss (tan δ) with frequency at a few selected temperatures. The inverse behavior of dielectric loss with the frequency is perceived because energy dissipation associated with polarization alters its direction with the applied electric field frequency, which consequently results in heating (Yadava et al. 2017). Relaxation peaks appeared at a particular temperature and frequency, when the frequency of applied field resonates with the hopping frequency of charge carriers [40]. The value of dielectric loss for BTO-BT nanocomposite are found to be 1.62 at 313 K and 100 Hz, which are comparable to each other. Figure 3.15b displays plots of dielectric loss (tan δ) with temperature at 100 Hz, 1 kHz, 10 kHz and 100 kHz frequencies for BTO-BT nanocomposite. It is lucid from figure 3.15 that the value of tan δ for material at 10 kHz firstly increases and attains maximum value, then it decreases swiftly. Such variation again directs toward the presence of Maxwell Wagner relaxation, which further indicates diffuse phase transition [35].

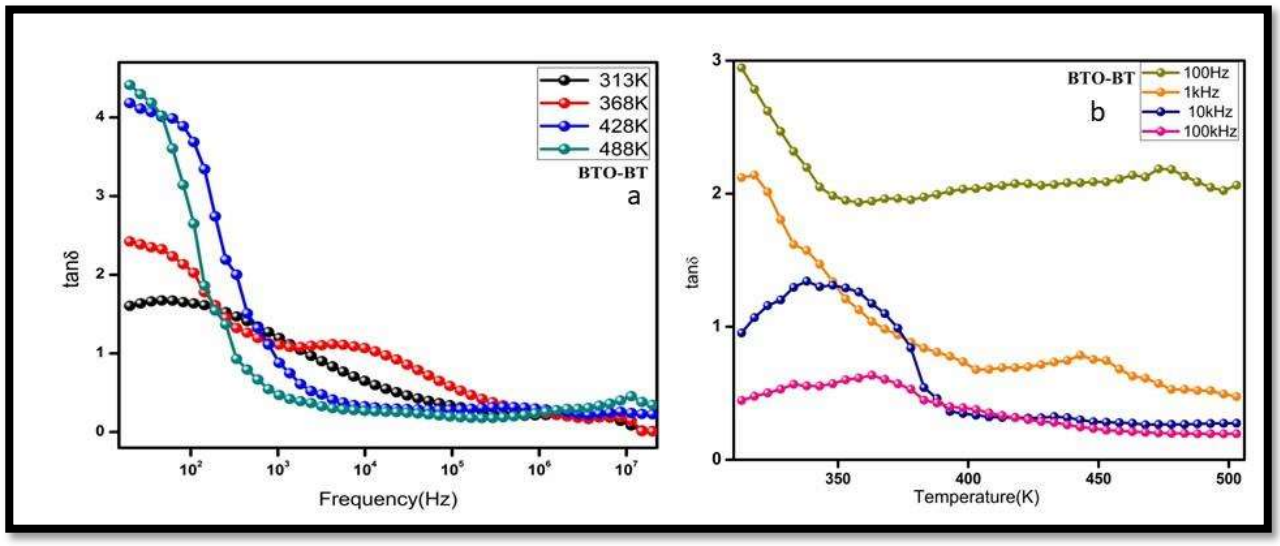

Figure 3.18 (a) -Dielectric loss (tanδ) as a function of frequency and (b)- Dielectric loss (tanδ)) as a function of temperature for BTO-BT nanocomposite.

3.8 Bandgap Analysis

Bandgap analysis is crucial for interpreting the mechanism of photocatalysis and determining which portion of solar radiation is useful for the procedures. Employing the data from UV-DRS, Tauc's plot was constructed to determine the bandgap for BTO-BT nanocomposite using the following relation.

$$(\boldsymbol{\alpha h\nu})^{1/n} = (\boldsymbol{h\nu - E_g}) \qquad (3.\ 12)$$

In equation 12, α symbolizes the molar absorption coefficient. The value of exponent n is 1/2 for the direct transition (Viezbicke et al. 2015). Figure 3.19 reveals the optical band gap (Eg), which is represented by the intercept of the linear fit on the x-axis(hν), which corresponds to 3.4 eV. This bandgap indicates the utilization of UV radiation for the photocatalysis.

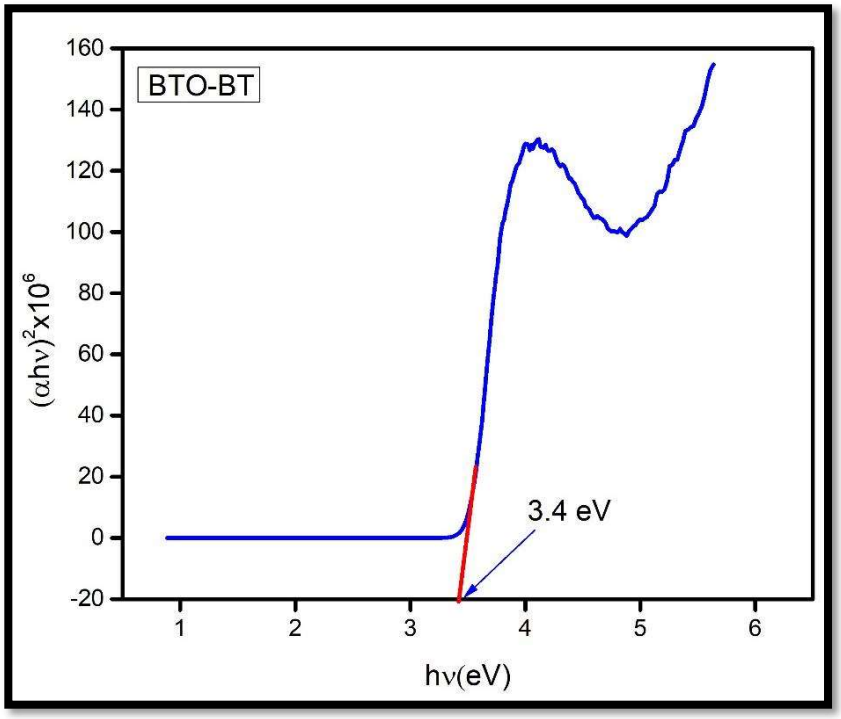

Figure 3.19 Tauc's Plot for BTO-BT nanocomposite

3.9 BET Surface Area Analysis

The nitrogen adsorption-desorption isotherms have been used to acquire information regarding BET specific surface area of BTO-BT nanocomposite and its pore size distribution. The nitrogen adsorption-desorption isotherm of BTO-BT nanocomposite exhibited hysteresis loop at a relative pressure (P/P_o) close to unity is shown in figure 3.20, indicating the presence of mesoporous structure which can be assorted as type IV with characteristic H3-shaped hysteresis loops according to IUPAC classification (Kruk and Jaroniec 2001).The H3 hysteresis loop is associated with slit-like pores formed by pellets-like grains, as can be visualized by SEM analysis (Xiang et al. 2011). The BET specific surface area of BTO-BT nanocomposite is 1.679 m^2g^{-1}. The inset of the figure displays the BJH pore size distribution curves derived from the desorption branch. BJH pore size distribution is broad in the range, indicating the presence of

mesopores and macropores with maximum pores in the range of 10~30 nm. A pore of diameter within 1–100 nm limits are mesopores which are many times the diameter of adsorbate molecules, will exhibit capillary condensation and it is proved that capillary condensation enhances the photocatalytic activity (Kim and Ehrman 2009; Hall et al. 2012).

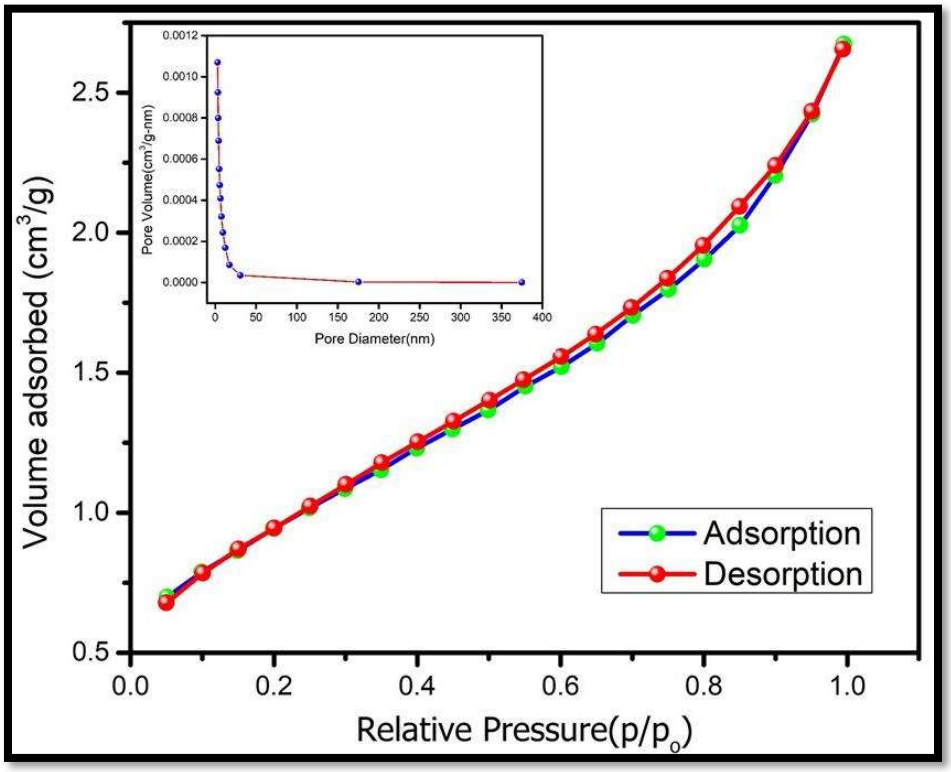

Figure 3.20 N_2 adsorption-desorption isotherms and the inset corresponding to pore-size distribution curves for BTO-BT nanocomposite

3.10 Photocatalytic efficiency

The photocatalytic activity of the as-synthesized BTO-BT sample was evaluated by degradation of typical organic waste Rhodamine B (RhB) under solar light irradiation. Figure 3.21(a) shows the UV-Vis. Absorbance spectra for the degradation of RhB in the presence of BTO-BT. There is no significant degradation of RhB was observed in the absence of BTO-BT photocatalyst. The BTO-BT photocatalyst degrades almost 43% of RhB dye in 60 minutes of the time period.

Figure 3.21(b) displays that the kinetic plot of $\ln(A_t/A_0)$ versus irradiation time for degradation of RhB, proving that the experimental data fitted well with first order kinetics. The k_{app} and correlation coefficient (R^2) was found to 0.0092 min^{-1} and 0.99, respectively, for the photodegradation of RhB with BTO-BT.

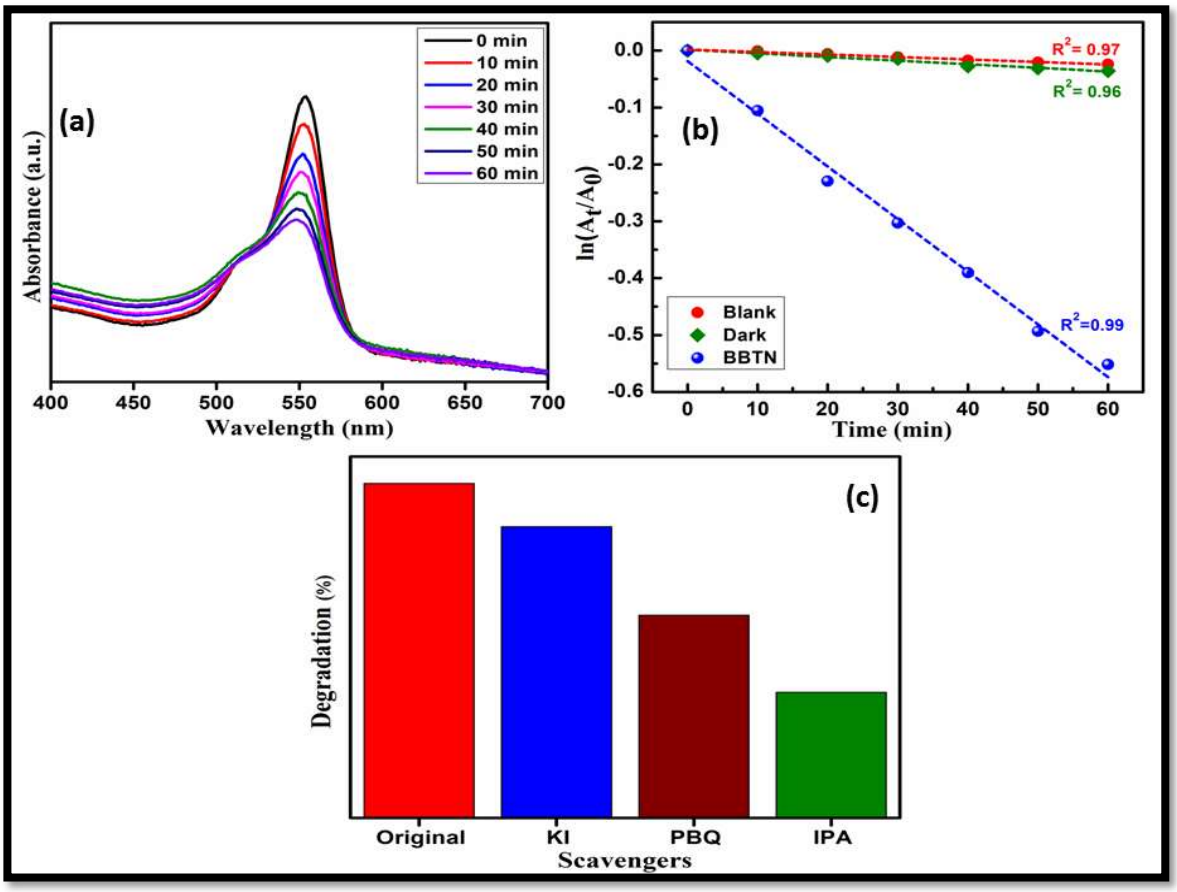

Figure 3.21 (a) Absorbance spectra of RhB degradation by BTO-BT, (b) Kinetic plot of RhB degradation by BTO-BT, (c) percentage degradation of RhB with different scavengers.

In the photocatalytic experiment, various active species like superoxide radical ($O_2^{\cdot-}$), hydroxyl radical ($OH^{\cdot-}$), and holes (h^+) contribute major role in the degradation of many organic recalcitrants. The scavengers like p-benzoquinone (PBQ), iso-propyl alcohol (IPA), and

potassium iodide (KI) were used to trap $O_2^{\cdot -}$ radicals, $OH^{\cdot}$ radicals, and holes (h^+) respectively formed during the degradation experiment. Figure 3.21(c) displays the result of scavenging experiments for BTO-BT. The graph shows that RhB degradation was greatly inhibited by IPA than other trapping agents. IPA also have a negative effect on the photodegradation of RhB while addition of KI display minimum negative effect over degradation of RhB. The above results show that $OH^{\cdot}$ radicals and $O_2^{\cdot -}$ are the major reactive species generated during the photocatalytic reaction. The order of active species generated during the catalytic experiment is $OH^{\cdot} > O_2^{\cdot -} > h^+$.

3.11 References

Arandiyan H, Dai H, Deng J, Liu Y, Bai B, Wang Y, Li X, Xie S, Li J. 2013. Three-dimensionally ordered macroporous La0.6Sr0.4MnO3 with high surface areas: Active catalysts for the combustion of methane. Journal of Catalysis. 307:327–339. doi:10.1016/j.jcat.2013.07.013.

Bantawal H, Krishna Bhat D. 2018. Hierarchical Porous Batio3 Nano-Hexagons as A Visible Light Photocatalyst. IJET. 7(4.5):105. doi:10.14419/ijet.v7i4.5.20022.

Barlow M. 1999. World Rivers Review. International Rivers Network, Berkeley.:6–7.

Benedek NA. 2015. Understanding ferroelectricity in layered perovskites: new ideas and insights from theory and experiments. 44(23). doi:10.1039/c5dt00010f.

Bhattacharya S, Maiti R, Sen MB, Saha SK, Chakravorty D. Anomalous enhancement in the magnetoconductance of graphene / CoFe 2 O 4 composite due to spin – orbit coupling. doi:10.1088/0022-3727/48/43/435002.

Chakrabarti K, Sarkar B, Ashok VD. 2013. Interfacial magnetism and exchange coupling in BiFeO 3 – CuO nanocomposite. doi:10.1088/0957-4484/24/50/505711.

Chu M-W, Ganne M, Caldes MT, Brohan L. 2002. X-ray photoelectron spectroscopy and high resolution electron microscopy studies of Aurivillius compounds: Bi 4- x La x Ti 3 O 12 (x= 0, 0.5, 0.75, 1.0, 1.5, and 2.0). Journal of applied physics. 91(5):3178–3187.

Delekar SD, Yadav HM, Achary SN, Meena SS, Pawar SH. 2012. Structural refinement and photocatalytic activity of Fe-doped anatase TiO 2 nanoparticles. Applied Surface Science. 263:536–545. doi:10.1016/j.apsusc.2012.09.102.

Feng S, Huang G. 2001. Effects of emulsifiers on the controlled release of paclitaxel (Taxol®) from nanospheres of biodegradable polymers. Journal of Controlled Release.:17.

Galasso FS, Kestigan M. 2007. Bismuth Titanate, Bi 4 Ti 3 O 12 . :112–113. doi:10.1002/9780470132616.ch24.

Generic I, Squibb B, Index M, Index M. 1952. Chapter-1 Introduction. :1–61.

Gordani GR, Ghasemi A, Saidi A. 2014. Enhanced magnetic properties of substituted Sr-hexaferrite nanoparticles synthesized by co-precipitation method. Ceramics International. 40(3):4945–4952. doi:10.1016/j.ceramint.2013.10.096.

Hall MR, Tsang SCE, Casey SP, Khan MA, Yang H. 2012. Synthesis, characterization and hygrothermal behaviour of mesoporous silica high-performance desiccants for relative humidity

buffering in closed environments. Acta Materialia. 60(1):89–101. doi:10.1016/j.actamat.2011.09.016.

Henini M. 2010. Principles of Electronic Materials and Devices (Second Edition). Microelectronics Journal. 33(8):681. doi:10.1016/s0026-2692(02)00042-3.

Hou D, Luo W, Huang Y, Yu JC, Hu X. 2013. Synthesis of porous Bi4Ti3O12 nanofibers by electrospinning and their enhanced visible-light-driven photocatalytic properties. Nanoscale. 5(5):2028. doi:10.1039/c2nr33750a.

Jonscher AK. 1972. Department of Physics, Chelsea College, Pulton Place, London S.W.6, England. Journal of Non-Crystalline Solids. 10:293–315.

Ke Q, Lou X, Wang Y, Wang J. 2010. thin films. :1–7. doi:10.1103/PhysRevB.82.024102.

Kim S, Ehrman SH. 2009. Photocatalytic activity of a surface-modified anatase and rutile titania nanoparticle mixture. Journal of Colloid and Interface Science. 338(1):304–307. doi:10.1016/j.jcis.2009.06.047.

Kongmark C, Coulter R, Cristol S, Rubbens A, Pirovano C, Löfberg A, Sankar G, van Beek W, Bordes-Richard E, Vannier R-N. 2012. A Comprehensive Scenario of the Crystal Growth of γ-Bi_2MoO_6 Catalyst during Hydrothermal Synthesis. Crystal Growth & Design. 12(12):5994–6003. doi:10.1021/cg301070e.

Kruk M, Jaroniec M. 2001. Gas Adsorption Characterization of Ordered Organic−Inorganic Nanocomposite Materials. Chem Mater. 13(10):3169–3183. doi:10.1021/cm0101069.

Kumar A, Yadava SS, Gautam P, Khare A, Mandal KD. 2018. Magnetic and dielectric studies of barium hexaferrite (BaFe12O19) ceramic synthesized by chemical route. Journal of Electroceramics.:1–10. doi:10.1007/s10832-018-0146-x.

Liu G, Wang L, Yang HG, Cheng H-M, (Max) Lu GQ. 2010. Titania-based photocatalysts—crystal growth, doping and heterostructuring. J Mater Chem. 20(5):831–843. doi:10.1039/B909930A.

Liu Y, Zhang M, Li L, Zhang X. 2014. One-dimensional visible-light-driven bifunctional photocatalysts based on Bi4Ti3O12 nanofiber frameworks and Bi2XO6 (X=Mo, W) nanosheets. Applied Catalysis B: Environmental. 160–161:757–766. doi:10.1016/j.apcatb.2014.06.023.

May AF, McGuire MA, Sales BC. 2014. Effect of Eu magnetism on the electronic properties of the candidate Dirac material EuMnBi2. Physical Review B - Condensed Matter and Materials Physics. 90(7):1–7. doi:10.1103/PhysRevB.90.075109.

Moure A. 2018. Review and Perspectives of Aurivillius Structures as a Lead-Free Piezoelectric System. Applied Sciences. 8(1):62. doi:10.3390/app8010062.

Murugesan C, Sathyamoorthy B, Chandrasekaran G. 2015. Structural, dielectric and magnetic properties of Gd substituted manganese ferrite nanoparticles. Physica Scripta. 90(8). doi:10.1088/0031-8949/90/8/085809.

Naresh G, Mandal TK. 2014. Excellent Sun-Light-Driven Photocatalytic Activity by Aurivillius Layered Perovskites, Bi $_{5-x}$ La $_{x}$ Ti $_{3}$ FeO $_{15}$ (x = 1, 2). ACS Appl Mater Interfaces. 6(23):21000–21010. doi:10.1021/am505767c.

Nayak P, Badapanda T, Panigrahi S. 2015. Effect of sintering temperature on electrical properties of SrBi4Ti4O15 ceramics. Journal of Materials Science: Materials in Electronics. 26(5):2913–2920. doi:10.1007/s10854-015-2777-x.

Panchal G, Shukla DK, Choudhary RJ, Reddy VR, Phase DM. 2017. The effect of oxygen stoichiometry at the interface of epitaxial BaTiO $_{3}$ /La $_{0.7}$ Sr $_{0.3}$ MnO $_{3}$ bilayers on its electronic and magnetic properties. Journal of Applied Physics. 122(8):085310. doi:10.1063/1.5000133.

Rana S, Rawat J, Misra RDK. 2005. Anti-microbial active composite nanoparticles with magnetic core and photocatalytic shell: TiO2–NiFe2O4 biomaterial system. Acta Biomaterialia. 1(6):691–703. doi:10.1016/j.actbio.2005.07.007.

Rana S, Rawat J, Sorensson MM, Misra RDK. 2006. Antimicrobial function of Nd3+-doped anatase titania-coated nickel ferrite composite nanoparticles: A biomaterial system. Acta Biomaterialia. 2(4):421–432. doi:10.1016/j.actbio.2006.03.005.

Rana S, Srivastava RS, Sorensson MM, Misra RDK. 2005. Synthesis and characterization of nanoparticles with magnetic core and photocatalytic shell: Anatase TiO2–NiFe2O4 system. Materials Science and Engineering: B. 119(2):144–151. doi:10.1016/j.mseb.2005.02.043.

Rawat J., Rana S, Sorensson MM, Misra RDK. 2007. Anti-microbial activity of doped anatase titania coated nickel ferrite composite nanoparticles. Materials Science and Technology. 23(1):97–102. doi:10.1179/174328407X158488.

Rawat Jagdish, Rana S, Srivastava R, Misra RDK. 2007. Antimicrobial activity of composite nanoparticles consisting of titania photocatalytic shell and nickel ferrite magnetic core. Materials Science and Engineering: C. 27(3):540–545. doi:10.1016/j.msec.2006.05.021.

Sharma S, Singh MM, Rai US, Mandal KD. 2015. Rationalization of dielectric properties of nano-sized iron doped yttrium copper titanate using impedance and modulus studies. Materials Science in Semiconductor Processing. 31:720–727. doi:10.1016/j.mssp.2014.12.069.

Sharma S, Yadav SS, Singh MM, Mandal KD. 2014. Impedance spectroscopic and dielectric properties of nanosized Y 2/3 Cu 3 Ti 4 O 12 ceramic . Journal of Advanced Dielectrics. 04(04):1450030. doi:10.1142/s2010135x14500301.

Shukla Y, Srivastava, Bhatnagar, Singh, Mishra, Kumar, Gupta. 2013 Apr. Synthesis of PLGA nanoparticles of tea polyphenols and their strong in vivo protective effect against chemically induced DNA damage. IJN.:1451. doi:10.2147/IJN.S26364.

Sultan K, Ikram M, Gautam S, Lee HK, Chae KH, Asokan K. 2015. Electrical and magnetic properties of the pulsed laser deposited Ca doped LaMnO3 thin films on Si (100) and their electronic structures. RSC Advances. 5(85):69075–69085. doi:10.1039/c5ra08028b.

Sun D, Jin X, Liu H, Zhu J, Zhu Yudan, Zhu Yinyin. 2007. Investigation on FTIR spectrum of barium titanate ceramics doped with alkali ions. Ferroelectrics. 355(1):145–148.

Sunkara BK, Misra RDK. 2008. Enhanced antibactericidal function of W4+-doped titania-coated nickel ferrite composite nanoparticles: A biomaterial system. Acta Biomaterialia. 4(2):273–283. doi:10.1016/j.actbio.2007.07.002.

Tellier J, Boullay P, Manier M, Mercurio D. 2004. A comparative study of the Aurivillius phase ferroelectrics CaBi 4Ti4O15 and BaBi4Ti 4O15. Journal of Solid State Chemistry. 177(6):1829–1837. doi:10.1016/j.jssc.2004.01.008.

Thomas AK, Abraham K, Thomas J, Saban K V. 2017. Electrical and dielectric behaviour of Na 0.5 La 0.25 Sm 0.25 Cu 3 Ti 4 O 12 ceramics investigated by impedance and modulus spectroscopy. Journal of Asian Ceramic Societies. 5(1):56–61. doi:10.1016/j.jascer.2017.01.002.

Venkatasubramanian R, Srivastava RS, Misra RDK. 2008. Comparative study of antimicrobial and photocatalytic activity in titania encapsulated composite nanoparticles with different dopants. Materials Science and Technology. 24(5):589–595. doi:10.1179/174328408X282065.

Viezbicke BD, Patel S, Davis BE, Birnie DP. 2015. Evaluation of the Tauc method for optical absorption edge determination: ZnO thin films as a model system: Tauc method for optical absorption edge determination. Phys Status Solidi B. 252(8):1700–1710. doi:10.1002/pssb.201552007.

Wang T, Hu J, Yang H, Jin L, Wei X, Li C, Yan F, Lin Y. 2017. Dielectric relaxation and Maxwell-Wagner interface polarization in Nb2O5 doped 0.65BiFeO3-0.35BaTiO3 ceramics. Journal of Applied Physics. 121(8):0–9. doi:10.1063/1.4977107.

Xiang Q, Yu J, Jaroniec M. 2011. Enhanced photocatalytic H2-production activity of graphene-modified titania nanosheets. Nanoscale. 3(9):3670. doi:10.1039/c1nr10610d.

Yadava SS, Khare A, Gautam P, Kumar A, Mandal KD. 2017. Dielectric, ferroelectric and magnetic study of iron doped hexagonal Ba 4 YMn 3 O 11.5-:δ (BYMO) and its dependence on temperature as well as frequency. New Journal of Chemistry. 41(11):4611–4617. doi:10.1039/c6nj04071c.

Yoon S, Son K, Ebbinghaus SG, Widenmeyer M, Weidenkaff A. 2018. Ferromagnetism in nitrogen and fl uorine substituted BaTiO 3. 749:628–633. doi:10.1016/j.jallcom.2018.03.221.

Zhang L, Wang H, Chen Z, Wong PK, Liu J. 2011 May. Bi2WO6 micro/nano-structures: Synthesis, modifications and visible-light-driven photocatalytic applications. Applied Catalysis B: Environmental.:S0926337311002098. doi:10.1016/j.apcatb.2011.05.008.

Zhang X, Wang X, Wang Q, Ma X, Liu Chunming, Li P, Liu Cailong, Han Y, Ma Y, Gao C. 2018. Hydride ion (H -) transport behavior in barium hydride under high pressure. Physical Chemistry Chemical Physics. 20(13):8917–8923. doi:10.1039/c7cp08386f.

Zhao X, Yang H, Cui Z, Wang X, Yi Z. 2019. Growth Process and CQDs-modified Bi4Ti3O12 Square Plates with Enhanced Photocatalytic Performance. Micromachines. 10(1):66. doi:10.3390/mi10010066.

Zn P, Ti N, Crystal OS. 2017. Switching Characteristics and High-Temperature. :1–10. doi:10.3390/ma10040349.